Acoustic 3D least-squares reverse time migration using the energy norm

Daniel Rocha, Paul Sava & Antoine Guitton
Center for Wave Phenomena, Colorado School of Mines

SUMMARY

We propose a least-squares reverse time migration (LSRTM) that uses a proper imaging condition to obtain faster convergence rates when compared with similar methods using conventional imaging conditions. The proposed modeling and migration operators use spatial and temporal derivatives that attenuate acquisition artifacts and deliver a better representation of the reflectivity and scattered wavefields. We apply the method to two Gulf of Mexico (GOM) field datasets: a 2D towed-streamer benchmark dataset and a 3D ocean-bottom node (OBN) dataset. We show the improvement in resolution of the LSRTM images, as well as the superior convergence rate.

INTRODUCTION

Wavefield migration delivers an image of subsurface structure using wavefield extrapolation methods (Sun et al., 2003; Biondi, 2012). For complex geological settings, the two-way wave equation is generally used for extrapolation and the migration procedure is known as reverse time migration (RTM) (Baysal et al., 1983; McMechan, 1983; Lailly, 1983). In practice, however, data recordings are always incomplete and possibly aliased and irregular, causing wavefield migration to degrade image quality and resolution especially for greater depths (Zhang et al., 2015). Such degradation occurs because migration represents the adjoint operator of single-scattering modeling, and therefore it is not a good approximation of the inverse operator that correctly reverses propagation of seismic data (Claerbout, 1992).

Considering these imaging quality issues, least-squares migration (LSM) is proposed to deliver images with more accurate amplitudes, illumination compensation, and reduced footprint of the acquisition geometry (Chavent and Plessix, 1999; Nemeth et al., 1999; Kuhl and Sacchi, 2003; Aoki and Schuster, 2009). If the RTM engine is used for migration, the method is called least-squares reverse time migration (LSRTM) (Dai et al., 2010; Yao and Jakubowicz, 2012; Dai and Schuster, 2012; Dong et al., 2012). Least-squares migration involves a forward operator (modeling) and an adjoint operator (migration) to achieve an image that best explains the data at receivers with respect to an objective function. To achieve the least-squares solution, one generally employs gradient methods that decrease the objective function iteratively (Hestenes and Stiefel, 1952; Scales, 1987).

Because of the high computational cost of LSRTM, which is at least an order of magnitude greater than RTM, some authors suggest techniques that expedite convergence towards the true reflectivity model. For instance, a common procedure to obtain faster rates of convergence is to use an approximate of the Hessian matrix (Aoki and Schuster, 2009; Tang, 2009; Huang et al., 2016). Here, we demonstrate that modeling and migration operators based on an imaging condition that delivers more accurate amplitudes and attenuate artifacts, such as the one derived from the energy norm (Douma et al., 2010; Whitmore and Crawley, 2012; Brandsberg-Dahl et al., 2013; Pestana et al., 2013; Rocha et al., 2016) also expedites convergence. This migration operator attenuates low-wavenumber artifacts, delivering a better representation of subsurface reflectivity. The corresponding modeling operator uses spatial and temporal derivatives based on the wave equation itself to generate scattered wavefields from the energy image.

THEORY

We can define acoustic wavefield migration as

$$\mathbf{m} = \mathbf{L}^{\mathrm{T}}\mathbf{d}_r \ , \tag{1}$$

where $\mathbf{L}^{\mathrm{T}}$ is the migration operator based on some imaging condition, $\mathbf{d}_r$ is single-scattered data recorded at receiver locations, and $\mathbf{m}$ is an image (representing reflectivity). The operator $\mathbf{L}^{\mathrm{T}}$ involves back-propagation of $\mathbf{d}_r$ through an Earth model, thus generating a receiver wavefield $\mathbf{U}_r$, and the application of an imaging condition with the source wavefield $\mathbf{U}_s$. One generally considers the migration operator as the adjoint operator of linearized modeling, represented by operator $\mathbf{L}$

$$\mathbf{d}_r = \mathbf{L}\mathbf{m} \ , \tag{2}$$

which generates single-scattering data $\mathbf{d}_r$ at receiver locations using an image containing reflectors that act as sources under the action of the source wavefield $\mathbf{U}_s$. Therefore, we define $\mathbf{L}$ as an adjoint of a particular imaging condition, and $\mathbf{m}$ is not necessarily defined in terms of contrasts in the Earth model.

The conventional imaging condition is the correlation between source and receiver wavefields $\mathbf{U}_s$ and $\mathbf{U}_r$:

$$\mathbf{m} = \left(\mathbf{U}_s\right)^{\mathrm{T}}\mathbf{U}_r \ . \tag{3}$$

Since both wavefields are generated by extrapolation using an Earth model and truncated data at receivers, we can rewrite equation 3 as

$$\mathbf{m} = \left(\mathbf{E}_+\mathbf{K}_s\mathbf{d}_s\right)^{\mathrm{T}}\mathbf{E}_-\mathbf{K}_r\mathbf{d}_r \ , \tag{4}$$

where $\mathbf{E}_+$ and $\mathbf{E}_-$ are forward and backward extrapolator operators, and $\mathbf{K_s}$ and $\mathbf{K_r}$ are source and receiver injection operators. Then, we can express the conventional migration operator as

$$\mathbf{L}^{\mathrm{T}} = \left(\mathbf{E}_+\mathbf{K}_s\mathbf{d}_s\right)^{\mathrm{T}}\mathbf{E}_-\mathbf{K}_r = \mathbf{U}_s^{\mathrm{T}}\mathbf{E}_-\mathbf{K}_r \ , \tag{5}$$

and the modeling operator as

$$\mathbf{L} = \mathbf{K}_r^{\mathrm{T}}\mathbf{E}_+\left(\mathbf{E}_+\mathbf{K}_s\mathbf{d}_s\right) = \mathbf{K}_r^{\mathrm{T}}\mathbf{E}_+\mathbf{U}_s \ . \tag{6}$$

In other words, single-scattered data $\mathbf{d}_r$ are obtained by extraction at the receiver locations ($\mathbf{K}_r^{\mathrm{T}}$) of the wavefield extrapolated ($\mathbf{E}_+$) with $\mathbf{U}_s\mathbf{m}$ as the source term.

The energy imaging condition for acoustic isotropic wavefields $\mathbf{U}_s$ and $\mathbf{U}_r$ is defined as (Rocha et al., 2016)

$$\mathbf{m} = (\square\mathbf{U}_s)^{\mathrm{T}}\,\square\mathbf{U}_r\ , \tag{7}$$

where $\square$ is the energy operator

$$\square = \left\{\nabla, \frac{1}{v\,(\mathbf{x})}\frac{\partial}{\partial t}\right\}\ , \tag{8}$$

and $v\,(\mathbf{x})$ is the migration velocity. Using equation 4, equation 7 becomes

$$\mathbf{m} = (\square\mathbf{E}_+\mathbf{K}_s\mathbf{d}_s)^{\mathrm{T}}\,\square\mathbf{E}_-\mathbf{K}_r\mathbf{d}_r\ . \tag{9}$$

Since equation 9 is a function of $\mathbf{d}_r$, one can write the energy migration operator as

$$\mathbf{L}^{\mathrm{T}} = (\square\mathbf{E}_+\mathbf{K}_s\mathbf{d}_s)^{\mathrm{T}}\,\square\mathbf{E}_-\mathbf{K}_r = (\square\mathbf{U}_s)^{\mathrm{T}}\,\square\mathbf{E}_-\mathbf{K}_r\ , \tag{10}$$

and the energy modeling operator as

$$\mathbf{L} = \mathbf{K}_r^{\mathrm{T}}\mathbf{E}_+\square^{\mathrm{T}}\square\,(\mathbf{E}_+\mathbf{K}_s\mathbf{d}_s) = \mathbf{K}_r^{\mathrm{T}}\mathbf{E}_+\square^{\mathrm{T}}\square\mathbf{U}_s\ . \tag{11}$$

In other words, energy linearized modeling produces scattered wavefield using $\square^{\mathrm{T}}\square\mathbf{U}_s\mathbf{m}$ as the source term, which for a point in space and time can be written as

$$\begin{aligned}\left[\square^{\mathrm{T}}\square\mathbf{U}_s\mathbf{m}\right](\mathbf{x},t) &= \frac{\mathbf{m}\,(\mathbf{x})}{v^2\,(\mathbf{x})}\ddot{\mathbf{U}}_s\,(\mathbf{x},t)\\ &- \nabla\cdot\left[\mathbf{m}\,(\mathbf{x})\,\nabla\mathbf{U}_s\,(\mathbf{x},t)\right]\ .\end{aligned} \tag{12}$$

The same procedure to find a proper adjoint operator is applicable to other imaging conditions. For instance, applying a Laplacian operator on a conventional image is theoretically equivalent to the application of the imaging condition in equation 7 (Douma et al., 2010). Knowing that the Laplacian operator is self-adjoint, the imaging condition with Laplacian can be written as

$$\mathbf{m} = \nabla^2\,(\mathbf{U}_s)^{\mathrm{T}}\,\mathbf{U}_r\ . \tag{13}$$

The migration operator using the Laplacian is

$$\mathbf{L}^{\mathrm{T}} = \nabla^2\,(\mathbf{E}_+\mathbf{K}_s\mathbf{d}_s)^{\mathrm{T}}\,\mathbf{E}_-\mathbf{K}_r = \nabla^2\mathbf{U}_s^{\mathrm{T}}\mathbf{E}_-\mathbf{K}_r\ , \tag{14}$$

and the corresponding linearized modeling is written as

$$\mathbf{L} = \mathbf{K}_r^{\mathrm{T}}\mathbf{E}_+\,(\mathbf{E}_+\mathbf{K}_s\mathbf{d}_s)\,\nabla^2 = \mathbf{K}_r^{\mathrm{T}}\mathbf{E}_+\mathbf{U}_s\nabla^2\ . \tag{15}$$

EXAMPLES

To show how LSRTM with proper imaging conditions get faster convergence compared to conventional methods, we obtain convergence curves from a LSRTM experiment applied to a 2D GOM benchmark dataset, used by many authors in the past as a benchmark dataset (Dragoset, 1999; Guitton et al., 2012). Standard preprocessing is applied to the dataset prior to LSRTM, such as surface-related multiple suppression. We use 71 of the original 1001 shot records, resulting in a source spacing of approximately 267m. The shot decimation decreases the computational cost of the entire experiment but also introduces truncation artifacts, which are useful to test the effectiveness of the proposed LSRTM in attenuating acquisition artifacts. We test three modeling and migration operators for LSRTM: conventional (equations 5 and 6), Laplacian based (equations 14 and 15), and energy-norm based (equations 10 and 11). The objective functions (Figure 1b) of both alternative LSRTM's (energy and Laplacian) decrease faster than the one from conventional LSRTM, with the one based on energy decreasing slightly faster when compared to its Laplacian counterpart. Although the two alternative LSRTM's are theoretically equivalent, the discretization in wavefield extrapolation imposes more loss of accuracy of the numerical derivatives in image domain compared to wavefield domain. For illustration, we show the energy LSRTM image in Figure 1a. As suggested, the energy migration and modeling operators applied either on wavefield domain (equations 10 and 11) or on image domain in the form of a Laplacian operator (equations 14 and 15) provide faster convergence rates towards the final reflectivity model.

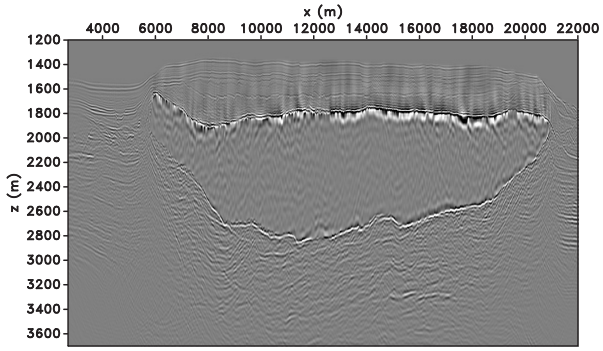

(a)

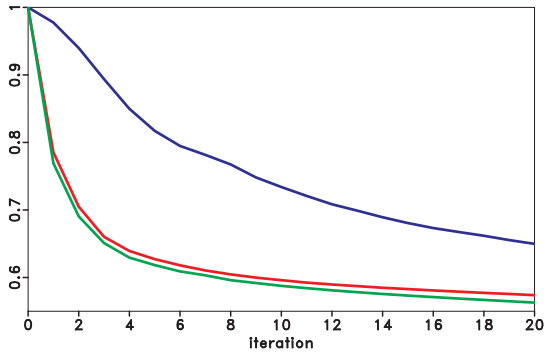

(b)

Figure 1: GOM benchmark dataset: (a) energy LSRTM image. (b) Normalized objective functions for conventional LSRTM (blue), LSRTM with Laplacian (red) and energy (green) operators. Both energy and Laplacian-based migration and modeling operators expedite convergence relative to using conventional operators.

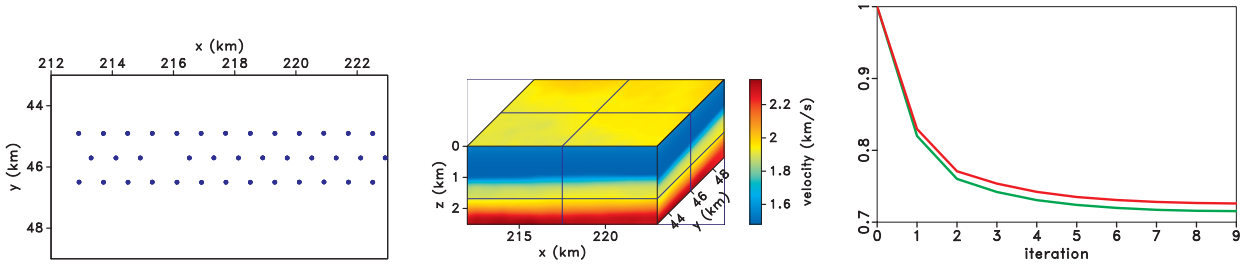

(a) (b) (c)

Figure 2: (a) GOM 3D dataset: 37 nodes spaced by approximately 800m, and sources densely distributed at the surface of the model. (b) Velocity model. (c) Normalized objective functions for Laplacian based (red) and energy-norm based (green) LSRTM's.

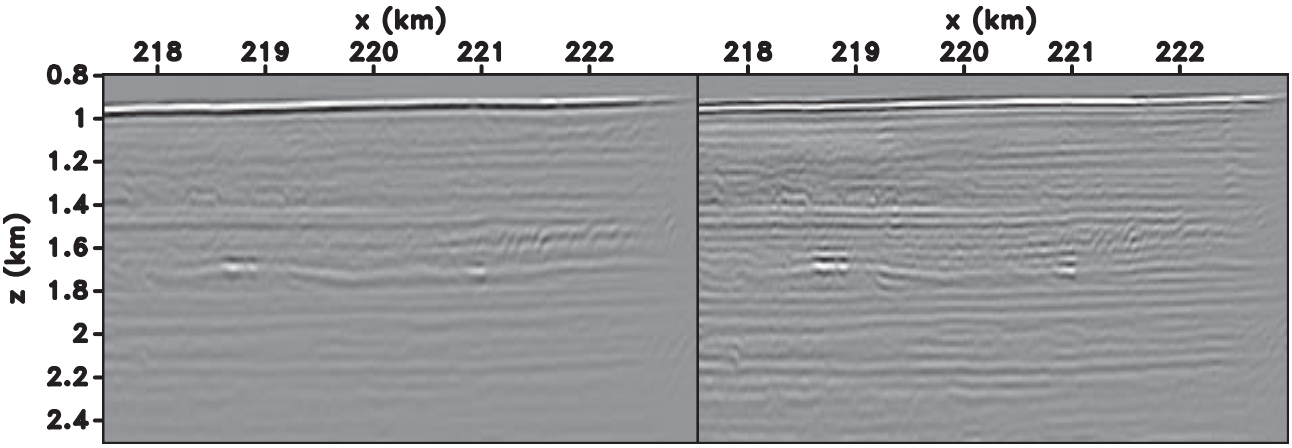

Figure 3: GOM 3D dataset: energy RTM (left) and LSRTM (right) images for the inline section at $y = 44.9$km. Note the increase in frequency content and illumination for the LSRTM image compared to RTM.

We apply our method to a 3D ocean-bottom node (OBN) dataset from the Gulf of Mexico. We process the dataset to obtain only the down-going pressure component and perform mirror imaging (Godfrey et al., 1998; Ronen et al., 2005) of shallow geological structures. We use 37 node gathers with sources densely distributed at the water surface (Figure 2a), and the velocity model used in shown in Figure 2b. Based on the fact that conventional LSRTM has a worse performance in the preceding example, we perform two LSRTM experiments: Laplacian based LSRTM and energy-norm based LSRTM, which has a slightly smaller objective function value over iterations compared to its Laplacian counterpart, similarly to the preceding example. Comparing with standard RTM, we show the final energy LSRTM image of an inline section in Figure 3, and zoomed depth-sliced images in Figure 4. The image in Figure 3 compares RTM and LSRTM images side-by-side, and shows the increase in illumination and frequency content (especially towards low frequencies) in the LSRTM image. With a number of iterations corresponding to two orders of magnitude of the standard RTM computational cost, we obtain LSRTM images that exhibit more focused diffractions and delineated structures as shown by the depth slices in Figure 4.

CONCLUSIONS

We demonstrate that using proper linearized modeling and migration operators expedites LSRTM, which suffers from high computational cost. We test modeling and migration operators based on the energy norm, and we obtain faster convergence rates in our inversion, since our operators attenuate artifacts that do not properly characterize subsurface reflectivity. Our field data examples shows the improvement in image quality by using an expedited LSRTM compared to regular RTM.

ACKNOWLEDGEMENTS

We thank the sponsors of the Center for Wave Phenomena, whose support made this research possible. We thank Shell Exploration and Production Company for permission to publish the results using the 3D Gulf of Mexico dataset. The reproducible numeric examples in this paper use the Madagascar open-source software package (Fomel et al., 2013) available at http://www.ahay.org.

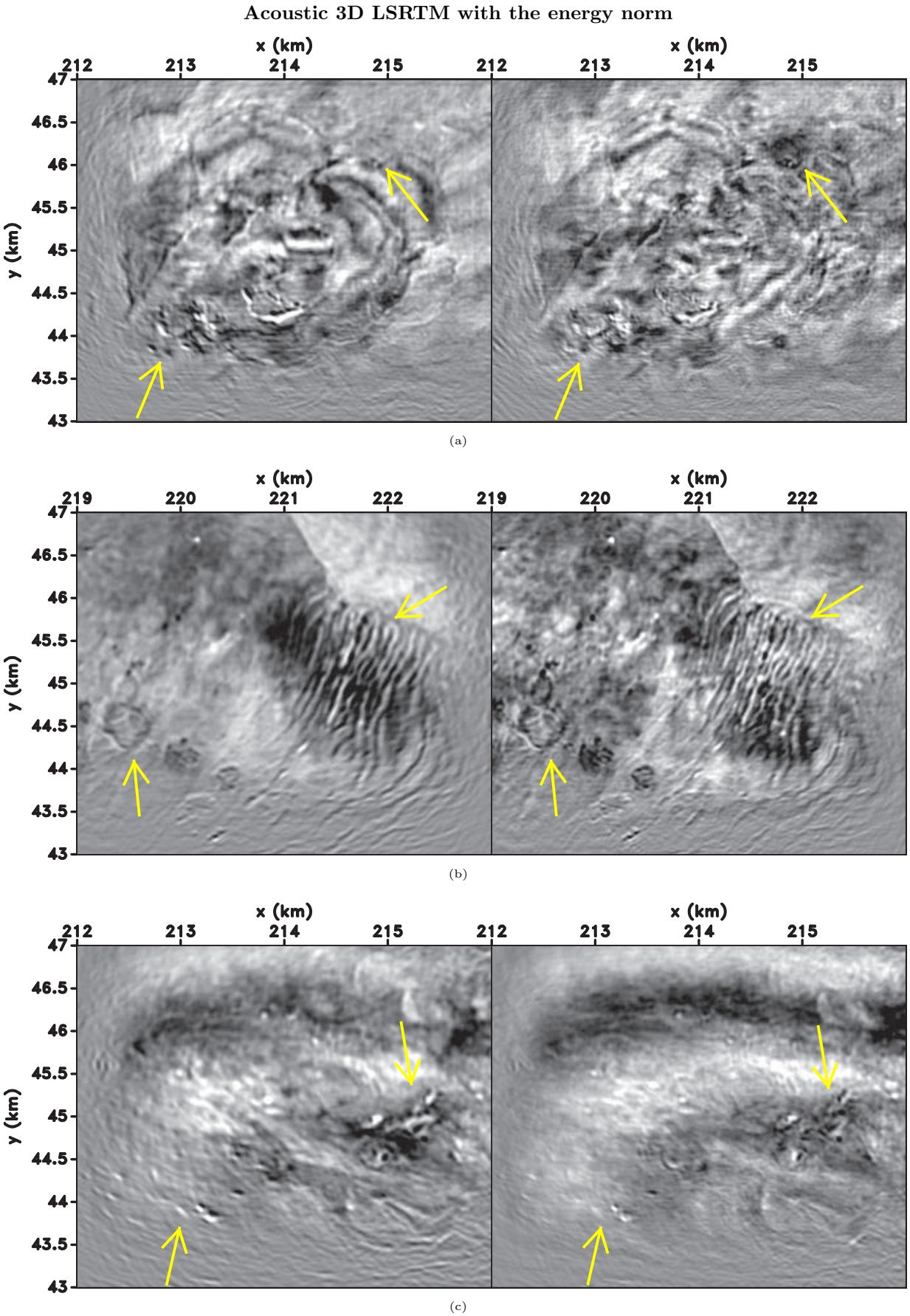

Figure 4: GOM 3D dataset: RTM (left) and LSRTM (right) images at (a) $z = 1.20$km, (b) 1.55km, (c) and 1.77km. The arrows indicate the greatest improvement in focusing of the diffractors and in delineation of the reflectors.

REFERENCES

Aoki, N., and G. T. Schuster, 2009, Fast least-squares migration with a deblurring filter: Geophysics, **74**, no. 6, WCA83–WCA93.

Baysal, E., D. D. Kosloff, and J. W. C. Sherwood, 1983, Reverse time migration: Geophysics, **48**, 1514–1524.

Biondi, B., 2012, *in* 4. Principles of Wavefield-continuation Migration: 39–50.

Brandsberg-Dahl, S., N. Chemingui, D. Whitmore, S. Crawley, E. Klochikhina, and A. Valenciano, 2013, 3D RTM angle gathers using an inverse scattering imaging condition: Presented at the 83rd Annual International Meeting, SEG, Expanded Abstracts, 3958–3962.

Chavent, G., and R.-E. Plessix, 1999, An optimal true–amplitude least–squares prestack depth–migration operator: Geophysics, **64**, 508–515.

Claerbout, J. F., 1992, Earth soundings analysis: Processing versus inversion: Blackwell Scientific Publications.

Dai, W., C. Boonyasiriwat, and G. Schuster, 2010, 3D multisource least-squares reverse-time migration: Presented at the 80th Annual International Meeting, SEG, Expanded Abstracts, 3120–3124.

Dai, W., and G. T. Schuster, 2012, Plane-wave Least-squares Reverse Time Migration: Presented at the 82rd Annual International Meeting, SEG, Expanded Abstracts.

Dong, S., J. Cai, M. Guo, S. Suh, Z. Zhang, B. Wang, and Z. Li, 2012, Least-squares reverse time migration: towards true amplitude imaging and improving the resolution: Presented at the 82rd Annual International Meeting, SEG, Expanded Abstracts.

Douma, H., D. Yingst, I. Vasconcelos, and J. Tromp, 2010, On the connection between artifact filtering in reverse-time migration and adjoint tomography: Geophysics, **75**, S219–S223.

Dragoset, B., 1999, A practical approach to surface multiple attenuation: The Leading Edge, **18**, 104–108.

Fomel, S., P. Sava, I. Vlad, Y. Liu, and V. Bashkardin, 2013, Madagascar: open-source software project for multidimensional data analysis and reproducible computational experiments: Journal of Open Research Software, 1:e8, DOI: http://dx.doi.org/10.5334/jors.ag.

Godfrey, R., P. Kristiansen, B. Armstrong, M. Copper, and E. Thorogood, 1998, Imaging the Foinaven ghost: Presented at the 68th Annual International Meeting, SEG, Expanded Abstracts, 1333–1335.

Guitton, A., G. Ayeni, and E. Daz, 2012, Constrained full–waveform inversion by model reparameterization: Geophysics, **77**, R117–R127.

Hestenes, M. R., and E. Stiefel, 1952, Methods of Conjugate Gradients for Solving Linear Systems: Journal of Research of the National Bureau of Standards, **49**, no. 6, 409–436.

Huang, W., P. Deng, and H.-W. Zhou, 2016, Least-squares reverse-time migration with hessian preconditioning: Presented at the 86th Annual International Meeting, SEG, Expanded Abstracts, 1043-1046.

Kuhl, H., and M. D. Sacchi, 2003, Least-squares wave-equation migration for AVO/AVA inversion: Geophysics, **68**, 262–273.

Lailly, P., 1983, The seismic inverse problem as a sequence of before stack migrations: Conference on Inverse Scattering, Theory and Application: Presented at the Society of Industrial and Applied Mathematics, Expanded Abstracts, 206–220.

McMechan, G. A., 1983, Migration by extrapolation of time dependent boundary values: Geophysical Prospecting, **31**, 413–420.

Nemeth, T., C. Wu, and G. T. Schuster, 1999, Least–squares migration of incomplete reflection data: Geophysics, **64**, 208–221.

Pestana, R., A. W. G. dos Santos, and E. S. Araujo, 2013, RTM imaging condition using impedance sensitivity kernel combined with Poynting vector: Presented at the 13th International Congress of The Brazilian Geophysical Society.

Rocha, D., N. Tanushev, and P. Sava, 2016, Acoustic wavefield imaging using the energy norm: Geophysics, **81**, no. 4, S151–S163.

Ronen, S., L. Comeaux, and X.-G. Miao, 2005, Imaging downgoing waves from ocean bottom stations: Presented at the 75th Annual International Meeting, SEG, Expanded Abstracts, 963–967.

Scales, J., 1987, Tomographic inversion via the conjugate gradient method: Geophysics, **52**, 179–185.

Sun, J., Y. Zhang, S. Gray, C. Notfors, and J. Young, 2003, 3-d prestack depth migration by wavefield extrapolation methods: Presented at the ASEG Extended Abstracts 2003, pp 1-4.

Tang, Y., 2009, Target-oriented wave-equation least-squares migration/inversion with phase–encoded hessian: Geophysics, **74**, no. 6, WCA95–WCA107.

Whitmore, N. D., and S. Crawley, 2012, Application of RTM inverse scattering imaging conditions: Presented at the 82nd Annual International Meeting, SEG, Expanded Abstracts, 1–6.

Yao, G., and H. Jakubowicz, 2012, Least-Squares Reverse-Time Migration: Presented at the 82rd Annual International Meeting, SEG, Expanded Abstracts.

Zhang, Y., L. Duan, and Y. Xie, 2015, A stable and practical implementation of least-squares reverse time migration: Geophysics, **80**, no. 1, V23–V31.